ARTICLES
PUBLISHED ONLINE: 24 AUGUST 2015 | DOI: 10.1038/NMAT4388
nature materials

Flexible high power-per-weight perovskite solar cells with chromium oxide–metal contacts for improved stability in air

Martin Kaltenbrunner[1]*, Getachew Adam[2], Eric Daniel Głowacki[2], Michael Drack[1], Reinhard Schwödiauer[1], Lucia Leonat[2], Dogukan Hazar Apaydin[2], Heiko Groiss[3], Markus Clark Scharber[2], Matthew Schuette White[2], Niyazi Serdar Sariciftci[2] and Siegfried Bauer[1]

Photovoltaic technology requires light-absorbing materials that are highly efficient, lightweight, low cost and stable during operation. Organolead halide perovskites constitute a highly promising class of materials, but suffer limited stability under ambient conditions without heavy and costly encapsulation. Here, we report ultrathin (3 μm), highly flexible perovskite solar cells with stabilized 12% efficiency and a power-per-weight as high as 23 W g^{-1}. To facilitate air-stable operation, we introduce a chromium oxide–chromium interlayer that effectively protects the metal top contacts from reactions with the perovskite. The use of a transparent polymer electrode treated with dimethylsulphoxide as the bottom layer allows the deposition—from solution at low temperature—of pinhole-free perovskite films at high yield on arbitrary substrates, including thin plastic foils. These ultra-lightweight solar cells are successfully used to power aviation models. Potential future applications include unmanned aerial vehicles—from airplanes to quadcopters and weather balloons—for environmental and industrial monitoring, rescue and emergency response, and tactical security applications.

Lightweight and flexible photovoltaic arrays with 130 μm thickness and 22% power conversion efficiency (PCE) are at present delivering energy to the Solar Impulse 2 airplane on its flight around the world[1]. Power-per-weight is the vital metric for this mission. Various other solar technologies for decentralized power generation and distribution, such as in blimps, weather balloons, robotic insects, smart buildings and aerospace applications have similar requirements. Critical features that will enable these future concepts to take off are the combination of high PCE, minimal weight, flexibility, mechanical resilience, operational stability and, ideally, low cost.

Promising materials with potential to meet these conditions include advanced silicon[2], ultrathin kesterites[3] (for example, CIGS, CZTS), organic semiconductors[4], II–VI and III–V inorganic semiconductors[5,6] and, most recently, organolead halide perovskites[7–9]. The rapid development of thin-film perovskites has now achieved power conversion efficiencies as high as 20% (refs 10,11). The high absorption coefficient allows the cells to be very thin, typically below 1 μm (ref. 12). The versatility in processing methods, including both solution[8,13] and vacuum-based techniques[7,14], potentially enables large flexibility in device design at low fabrication cost. Yet several significant problems remain before perovskite-based photovoltaics can be considered a viable technology for solar aviation, robotics and distributed power supply. Primarily the cells must conform to the physical criteria of weight and flexibility, meet reasonable fabrication yield, and show operational stability under ambient environment on the scale of days to weeks—and ultimately months and years—depending on the application.

In this work, we report planar perovskite solar arrays with a total thickness of 3 μm, including substrate, electrodes and a protective encapsulating layer. The cells show a stabilized PCE of 12%, a record power-per-weight of 23 W g^{-1}, and operate for days under normal environmental conditions. We fabricate these cells at low temperatures from low-cost materials at high yield.

Through the judicious selection of hole- and electron-transport layers and contact metals, we achieve a general approach for sandwiching an alkylammonium lead trihalide RNH_3PbX_3 perovskite active layer in a way to maximize performance and stability (Fig. 1a). Transparent, commodity-scale, and ultrathin 1.4-μm-thick PET foils serve as substrates to achieve photovoltaic devices with high power-per-weight, outstanding flexibility, and conformability at minimal cost. A layer of the conducting polymer poly(ethylenedioxythiophene):poly(styrene sulphonate) (PEDOT:PSS) with a sheet resistance of ∼105 Ω □$^{-1}$ forms the transparent, conductive, oxide-free and low-temperature processable hole selective electrode. Tuning of additives allows us to form a pinhole-free perovskite layer with uniform coverage even on rough plastic substrates. We process the methylammonium lead trihalide ($CH_3NH_3PbI_{3-x}Cl_x$, which we call MAPI for brevity) perovskite absorber layer in a printing-compatible manner by a one-step solution precursor deposition method. Critical to achieving high-efficiency devices in high yield is the subsequent deposition of a conformal and chemically inert electron-transporting material. We use vacuum-sublimed *N*,*N*′-dimethyl-3,4,9,10-tetracarboxylic perylene diimide (PTCDI) or solution-processed 6,6-phenyl C_{61} butyric acid methylester (PCBM). Chemical structures of all materials employed are found in Supplementary Fig. 1. The stability of the metal top contact is vital for performance and lifetime—we show that the deposition of chromium results in devices with very promising ambient air stability while operating at their maximum power

[1]Department of Soft Matter Physics, Johannes Kepler University Linz, Altenbergerstrasse 69, 4040 Linz, Austria. [2]Linz Institute for Organic Solar Cells (LIOS), Institute of Physical Chemistry, Johannes Kepler University Linz, Altenbergerstrasse 69, 4040 Linz, Austria. [3]Institute of Semiconductor and Solid State Physics, Johannes Kepler University Linz, Altenbergerstrasse 69, 4040 Linz, Austria. *e-mail: martin.kaltenbrunner@jku.at

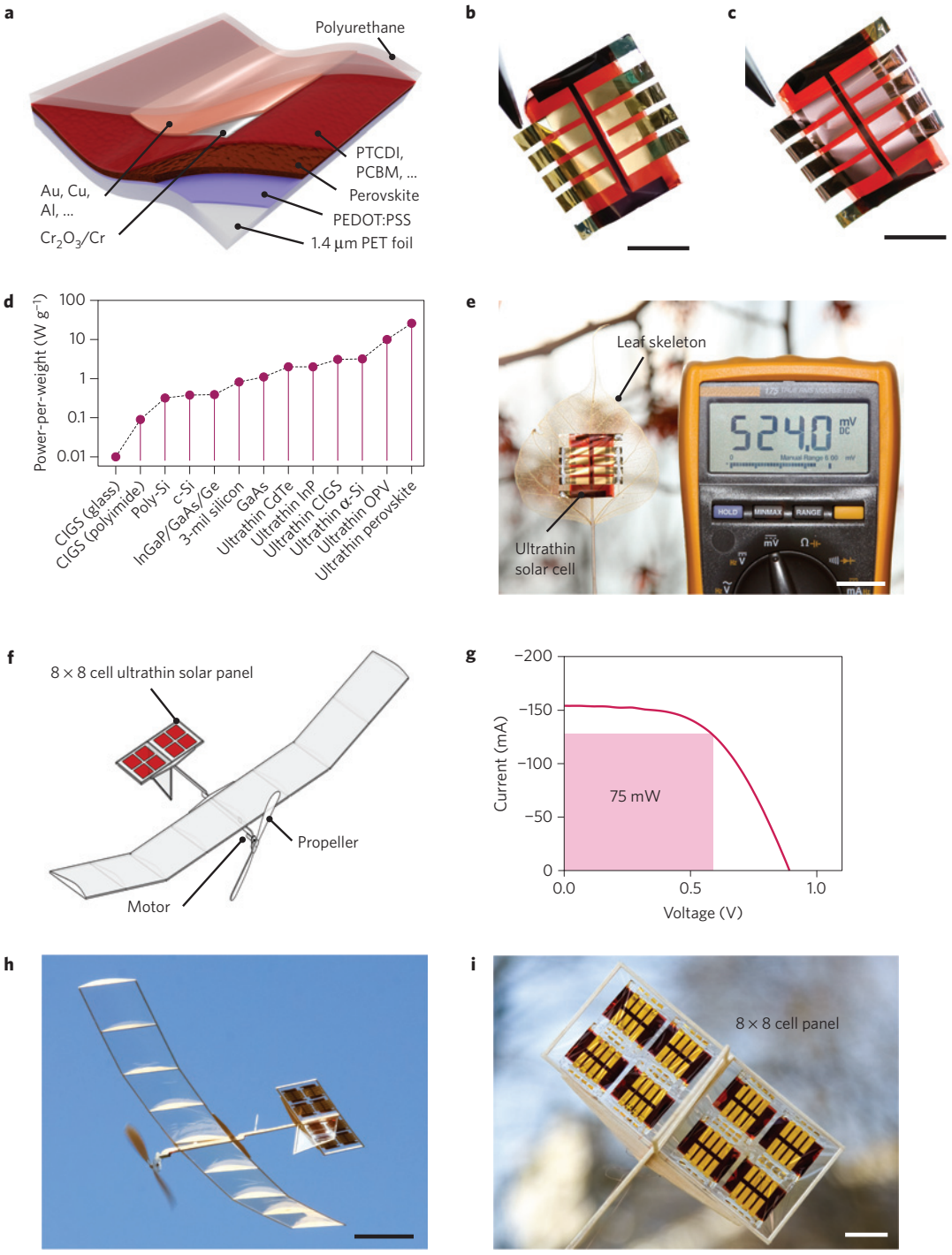

Figure 1 | Ultrathin and light perovskite solar cells. a, Schematic of the solar cell stack. 1.4-μm-thick PET foils serve as substrate, PEDOT:PSS is the transparent hole selective electrode. DMSO as additive promotes pinhole-free perovskite layer formation. The MAPI absorber is formed by a one-step solution precursor deposition method. PTCDI or PCBM are suitable electron-transport layers. A chromium layer with accompanying Cr_2O_3 stabilizes the metal top contact for operation in ambient air. Low-resistivity metals, for example, gold, copper and aluminium, complete the device. Optionally, PU serves as a 1-μm-thick capping layer for mechanical protection. **b**, Freestanding 3-μm-thick solar cells with gold top metal. Scale bar, 1 cm. **c**, Perovskite solar foil with low-cost copper back contacts. Scale bar, 1 cm. **d**, Power-per-weight of ultrathin perovskite solar cells is more than double the nearest competing photovoltaic technology. The 2-μm-thick cells (3 μm with PU capping) weigh only 4.6 g m^{-2} (5.2 g m^{-2} with PU) and have a power-per-weight of 26 W g^{-1} (23 W g^{-1} with PU). Cell data compared from published academic results of leading lightweight solar cells (details in the Methods and Supplementary Information). **e**, Dried leaf skeleton covered with a solar array of eight cells. The solar leaf (with a 100 Ω load) delivers ~2.75 mW under ~30 klx solar irradiance (Supplementary Movie 1). Scale bar, 2 cm. **f**, Schematic drawing of the solar-powered model airplane. The ultralight solar panel is integrated on the horizontal stabilizers (red rectangles) and powers a d.c. motor with propeller. **g**, Power output of the 64-cell solar panel. Under simulated AM 1.5 solar irradiance, the panel outputs 75 mW at MPP and powers the d.c. motor of our aviation model effectively under ambient outdoor illumination (~40 klx). **h**, Snapshot of the model plane during solar-powered outdoor flight (Supplementary Movie 3). Scale bar, 10 cm. **i**, Close-up photograph of the horizontal stabilizer with integrated solar panel. Scale bar, 2 cm.

point (MPP). Under our experimental conditions (see Methods), passive chromium(III) oxide (Cr_2O_3) is formed, confirmed by X-ray photoelectron spectroscopy (XPS, Supplementary Fig. 2). Moreover, chromium of different oxidation state and halides in the interlayer are also excluded by XPS. Cr_2O_3 effectively shields the commonly used metal contacts—for example, gold, silver, aluminium, and so on—from detrimental reactions with oxidizing and halide-forming iodide species. Gold, or the low-cost alternatives copper or aluminium, are deposited to complete the top contact. Optionally, a commercial spray-coatable polyurethane (PU) resin serves as a 1-μm-thick capping layer for mechanical protection. All process steps are compatible with standard semiconductor industry fabrication techniques, and require no inert atmosphere. The maximum processing temperature used is 110 °C. Freestanding 3-μm-thick perovskite arrays with top Cr/Au and Cr/Cu electrodes (Fig. 1b and c, respectively) have a stabilized PCE of 12% at a weight of 5.2 g m^{-2} (4.6 g m^{-2} without PU capping). This equates to a specific weight (watts produced under AM1.5 1,000 W m^{-2} irradiation/Weight) of 23 W g^{-1} (26 W g^{-1} without PU), which is the current record value for any photovoltaic technology (Fig. 1d) and compares favourably to other power-generating technologies such as electric motors (0.3–8.4 W g^{-1}) and heat engines/heat pumps (0.03 W g^{-1} up to 10 W g^{-1} for a jet engine, excluding fuel)[15].

Our solar foils form the base for outdoor demonstrations: a dried leaf skeleton covered with a solar cell, a solar-powered blimp, and an ultra-lightweight aviation model. Deployment of the ultrathin perovskite arrays in these applications underscores their ambient stability, conformability and high device fabrication yield. All demonstrations were carried out during midwinter afternoons in Austria (48° N) with roughly 30 to 40 kilolux (klx) solar irradiance, accentuating the applicability in sub-optimal solar conditions. The solar leaf (Fig. 1e, details are found in Supplementary Fig. 3 and online Supplementary Movie 1) is connected to a 100 Ω load and delivers approximately 2.75 mW (∼30 klx solar irradiance). Integration of such technological thin films with biological skeletal structures, including leaves and insect wings or exoskeletons, could pave the way for self-powered micro-aerial robotics or observation stations hidden from both birds in the tree canopies and people on the forest floor.

Unmanned aerial vehicles, with forms varying from airplanes to quad-copters to weather balloons, are major emerging technologies vital for environmental and industrial monitoring, rescue and emergency response, and tactical security applications. Future innovations in this field will be fuelled by the development of increasingly efficient lightweight high-energy-density power sources. We demonstrate the viability of ultrathin perovskite solar foils for aeronautic applications with lab-scale models. Two 4 × 8 solar modules are used to power a d.c. electrical motor with propeller while being directly integrated onto the curved hull of a lighter-than-air dirigible (see Supplementary Fig. 4 and Supplementary Movie 2) or the horizontal stabilizers of a model airplane (Fig. 1f–i and Supplementary Fig. 5 and Supplementary Movie 3). We fabricate solar modules on 1.4 μm foil based on 64 individual cells (Fig. 1h,i). Because of the excellent device yield afforded by the device stack, it is possible to make multiple modules of this type with 100% of the individual cells working. Such modules output 75 mW at MPP (Fig. 1g and Supplementary Fig. 4) under simulated AM 1.5 solar irradiance (∼8.4% efficiency normalized to active area), and power the d.c. motors of our aviation models effectively under ambient outdoor illumination (∼40 klx solar irradiance).

A high device yield is achieved by the formation of uniform and continuous pinhole-free perovskite thin films over large areas[16,17]. Rough and unconventional substrates, such as ultrathin plastic foils, pose additional challenges, especially as they place boundary conditions on processing techniques and parameters. We chose to optimize a one-step precursor deposition method to obtain high-performance MAPI films: methylammonium iodide is dissolved with PbI_2 and $PbCl_2$ in dimethylformamide. We find that spin coating these solutions onto PEDOT:PSS films treated with dimethylsulphoxide (DMSO) affords pinhole-free films over several-cm^2 areas. The quality of the resultant perovskite films strongly correlates with the content of DMSO added to the PEDOT:PSS, as is apparent from diascopic (transmitted) illumination optical microscopy images (Fig. 2a). MAPI films prepared on DMSO-free PEDOT:PSS surfaces are not continuous and exhibit micrometre-sized pinholes. By increasing the DMSO content in the PEDOT:PSS casting solution, the concentration and size of pinholes decreases. With 5–10% DMSO content, closed and uniform polycrystalline films are formed. DMSO acts as a solvent of the MAPI precursors and mediates the nucleation and crystallization at the PEDOT:PSS surface. The process is optimized on glass substrates (images in Fig. 2a), and leads to identically uniform films on the ultrathin PET substrates (Fig. 2b and Supplementary Fig. 6). Scanning electron microscopy (SEM) of MAPI films on PEDOT:PSS-coated foil (Fig. 2c) and corresponding atomic force microscopy (AFM) images (Supplementary Fig. 7) reveal tightly packed crystallites of several micrometres in size. X-ray diffraction evidences the formation of a tetragonal perovskite phase[18] on both glass coated with indium tin oxide (ITO) and foil substrates (Supplementary Fig. 8).

The MAPI photovoltaic cells must be completed with an electron-selective contact to complement the underlying PEDOT:PSS. As thermally evaporated chromium provides electron selectivity[19], devices using a Cr_2O_3/Cr top contact show a reasonable PCE of 7–8% (Supplementary Fig. 9). Electron-selective/hole-blocking solution-processed and vacuum-processed n-type interlayers PCBM and PTCDI greatly improve device performance and allow the fabrication of diodes with excellent rectification and low reverse-bias dark currents. PTCDI is a low-cost commercial pigment, highly resistant to degradation/bleaching and supports electron transport with $\mu_e \sim 1$–10 cm^2 V^{-1} s^{-1} (refs 20,21). Its deep highest occupied molecular orbital (HOMO) level results in effective hole-blocking and outstanding ambient stability. Vacuum-evaporated PTCDI produces homogeneous closed films over large areas, accounting for the exceptional device yield. Alternatively, PCBM is used as a solution-processable n-type buffer layer[22]. The deposition of an approximately 10 nm Cr layer with its accompanying oxide significantly improves air stability and facilitates the use of metal electrodes such as Au, Cu or Al under ambient conditions. The cross-sectional transmission electron microscopy (TEM) image of the device stack on foil (Fig. 2d) exhibits uniform, well-separated layers identical to the reference stacks on glass/ITO (Supplementary Fig. 10). Current density–voltage (J–V) scans under 1,000 W m^{-2} simulated solar illumination (Fig. 2e) give short-circuit currents (J_{SC}) of 17.5 ± 1 mA cm^{-2}, an open-circuit voltage (V_{OC}) of 930 ± 40 mV and an excellent fill factor (FF) of ∼80% on glass/ITO and ∼76% on foil. This corresponds to a PCE of 12.5 ± 1% for the reference cells on glass and 12 ± 1% on ultrathin foils. The reported uncertainties are larger than the standard deviation for a batch process of over ten optimized samples with eight individual cells to account for potential uncertainties in the measurement. We typically achieve 100% device yield when using PTCDI as n-type interlayer, and performance metrics for 21 ultrathin solar foils with eight cells each (168 individual solar cells) are found in Supplementary Fig. 11. Short-circuit currents from J–V measurements are in good agreement with the calculated J_{SC} obtained by integrating the external quantum efficiency (EQE) (Supplementary Fig. 12). Despite the rough surface of ultrathin PET foils (AFM measurements reveal ∼23 nm root mean square, Supplementary Fig. 7), excellent diode characteristics with reverse-bias current densities as low as 10 nA cm^{-2} at −0.5 V are achieved on foil, on par with reference diodes on smooth glass/ITO (Fig. 2f).

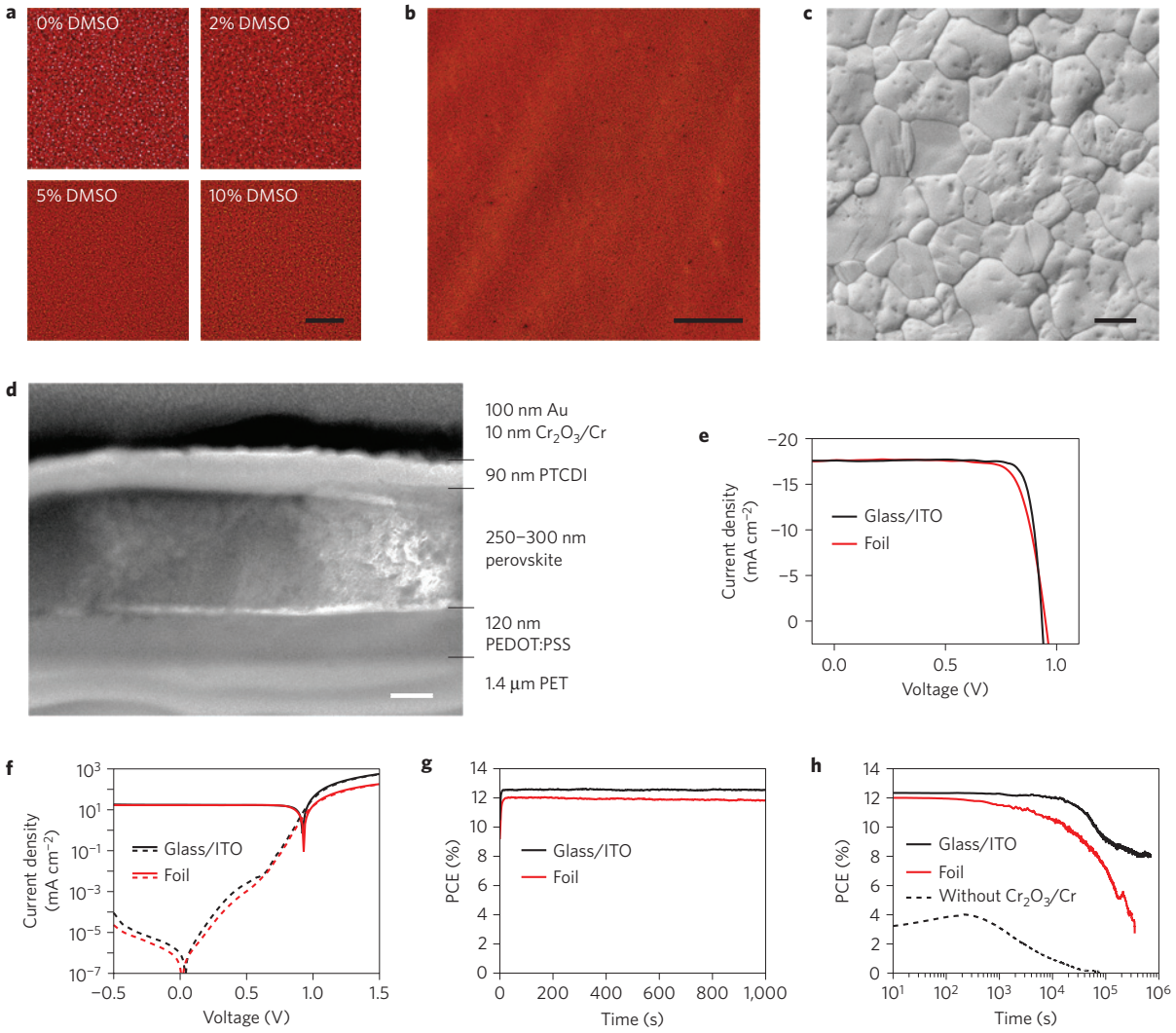

Figure 2 | Solar cell characterization. a, Additives in the PEDOT:PSS precursor mediate MAPI film formation. MAPI films on DMSO-free PEDOT:PSS (0% DMSO) are not continuous, showing micrometre-sized pinholes (white spots). At 2% DMSO content in the PEDOT:PSS solution, pinholes decrease in concentration and size. With 5–10% DMSO content, closed, uniform polycrystalline films form. Scale bar, 50 μm. **b**, Diascopic illumination optical microscopy image of DMSO-mediated uniform MAPI film on ultrathin PET. Scale bar, 200 μm. **c**, SEM image of MAPI film on PEDOT:PSS-coated foil, revealing tightly packed crystallites of several micrometres in size. Scale bar, 1 μm. **d**, TEM image of the device stack on foil, exhibiting uniform, well-separated layers. Scale bar, 100 nm. **e**, *J*–*V* scan under 1,000 W m^{-2} simulated solar illumination. A J_{SC} of 17.5 ± 1 mA cm^{-2}, V_{OC} of 930 ± 40 mV and FF of ~80% on glass/ITO (black trace) and ~76% on foil (red trace) correspond to a PCE of 12.5 ± 1% on glass and 12 ± 1% on foil. **f**, Diode characteristics on glass/ITO (black traces) and foil (red traces) under AM 1.5 irradiation (solid lines) and in the dark (dashed lines). Reverse-bias current densities of 10 nA cm^{-2} at −0.5 V are achieved on foil and on glass/ITO. **g**, Operation in ambient air. MPP tracking with stable power output at a PCE of 12.5% on glass/ITO (black trace) and 12% on foil (glass-supported, red trace) over 1,000 s. **h**, Subsequent longer-term MPP tracking in air under continuous illumination for freestanding foils (red trace) and a glass/ITO reference (black solid trace). The Cr/Cr_2O_3 interlayer greatly enhances air stability. Limited water barrier properties of PET cause a faster drop in performance, 80% of the initial PCE is retained after 10 h, and devices remain functional after four days of continuous operation. Glass/ITO cells without Cr_2O_3/Cr have <4% initial PCE that rapidly drops below 2% (dashed black line).

The MAPI perovskite is an ionic crystal, therefore frequency-dependent electrical polarization and ionic drift currents may affect potentiodynamic measurements[23,24]. We observe a scan-rate-dependent hysteresis in the current–voltage curves of devices employing PTCDI (Supplementary Fig. 13). Few reports demonstrate operational stability in ambient atmosphere of unsealed perovskite solar cells[25,26], all of which employ carbon-based electrodes as back contact. In our solar cells, we work with different contact metals (Au, Cu and Al) and use long-term MPP tracking in air to approximate real-world photovoltaic applications. Using a power-point-tracking computer program, we find stable power output at a PCE of 12.5% on glass/ITO and 12% on ultrathin foil (glass-supported) over the course of 1,000 s in air for both Cr/Au (Fig. 2g) and Cr/Cu contacts (Supplementary Fig. 14). The chromium oxide–chromium interlayer effectively suppresses detrimental effects of oxidative and halide-forming species on the metal contacts. Subsequent longer-term MPP tracking tests in air under continuous illumination for more than eight days reveal promising stability of the freestanding solar foils and their glass/ITO counterparts (Fig. 2h). Identical glass/ITO reference cells with gold top contacts, but without the Cr_2O_3/Cr interlayer, show a greatly reduced initial PCE of less than 4% once operated in ambient air that drops rapidly below 2% (Fig. 2h, dashed black line). MAPI solar cells with PCBM as the solution-processed ETL and Cr_2O_3/Cr–Au as metal contact show equally high-performance metrics (Supplementary Fig. 15) and enhanced stability in ambient air (Supplementary Fig. 16). The

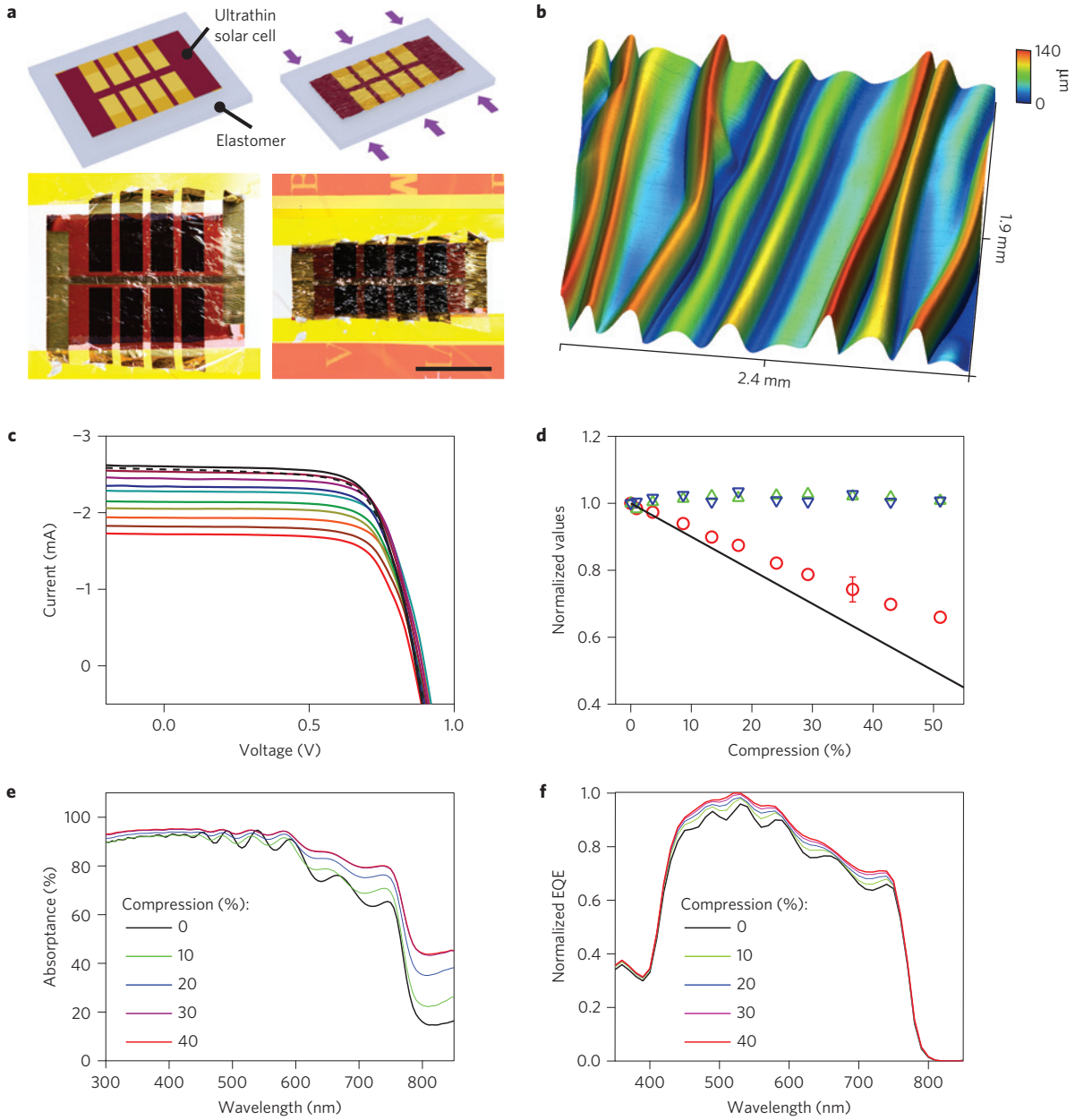

Figure 3 | Folds as light-trapping microstructures introduced by uniaxial compression. a, Schematic drawing and photographs of a stretchable perovskite solar cell. Sinusoidal waves and localized high-aspect-ratio ridge wrinkles form on relaxation of the pre-stretched elastomer. Photographs show a solar foil flat (left picture) and undergoing 50% compression (right picture). Scale bar, 1 cm. **b**, Three-dimensional map of the wrinkle morphology of a sample undergoing ~40% compressive strain. Roughly sinusoidal folds with wavelengths from 100 μm to 300 μm and peak amplitudes of up to 140 μm form. The active solar cell area exhibits multiple bends into radii of curvature down to 10 μm and less. **c**, *I*–*V* characteristics of a solar foil undergoing linear compression. Starting from a flat configuration (black solid trace), the cell is compressed in steps of ~10% down to 51% (equivalent to 100% tensile strain, red solid trace) and then re-flattened (dashed black trace). Viscoelasticity of the elastomer results in ~2% remanent compression. **d**, Solar cell performance metrics as a function of uniaxial compression. V_{OC} (blue downward triangles) and FF (green upward triangles) remain virtually unchanged when the device is compressed. I_{SC} (red circles) decreases as the illuminated active area shrinks. The measured decrease in photocurrent is less than expected from simple reduction of device area (solid black line). Wrinkles and folds function as light-trapping microstructures. Error bars in the J_{SC} metric represent statistical variations over three separate devices. **e**, Transmission/reflection spectra of a solar foil without top metal contacts. The absorptance increases as the foils are compressed and the micro-texture is forming. More light is absorbed across the relevant range of wavelengths, especially in the region between the absorption onset and 600 nm. **f**, EQE measurements of a solar foil undergoing quasi-linear compression. The enhancement of quantum efficiency for the compression-textured solar foils further corroborates the power-enhancing effect of micro-texturing the active cell area.

solution deposition of PCBM was not fully optimized, resulting in a device yield of 75% (typically six out of eight operational contacts per substrate). PCBM is nevertheless a promising electron-transport layer, enabling scan-rate-independent hysteresis-free MAPI solar cells (Supplementary Fig. 15).

The evaporation of a chromium film is critical to achieving air-stable devices. Solar cells with aluminium or gold in direct contact with the n-type buffer layer (PCBM or PTCDI) degrade immediately on exposure to ambient atmosphere. The ingress of H_2O into the MAPI results in the perovskite crystal structure degrading,

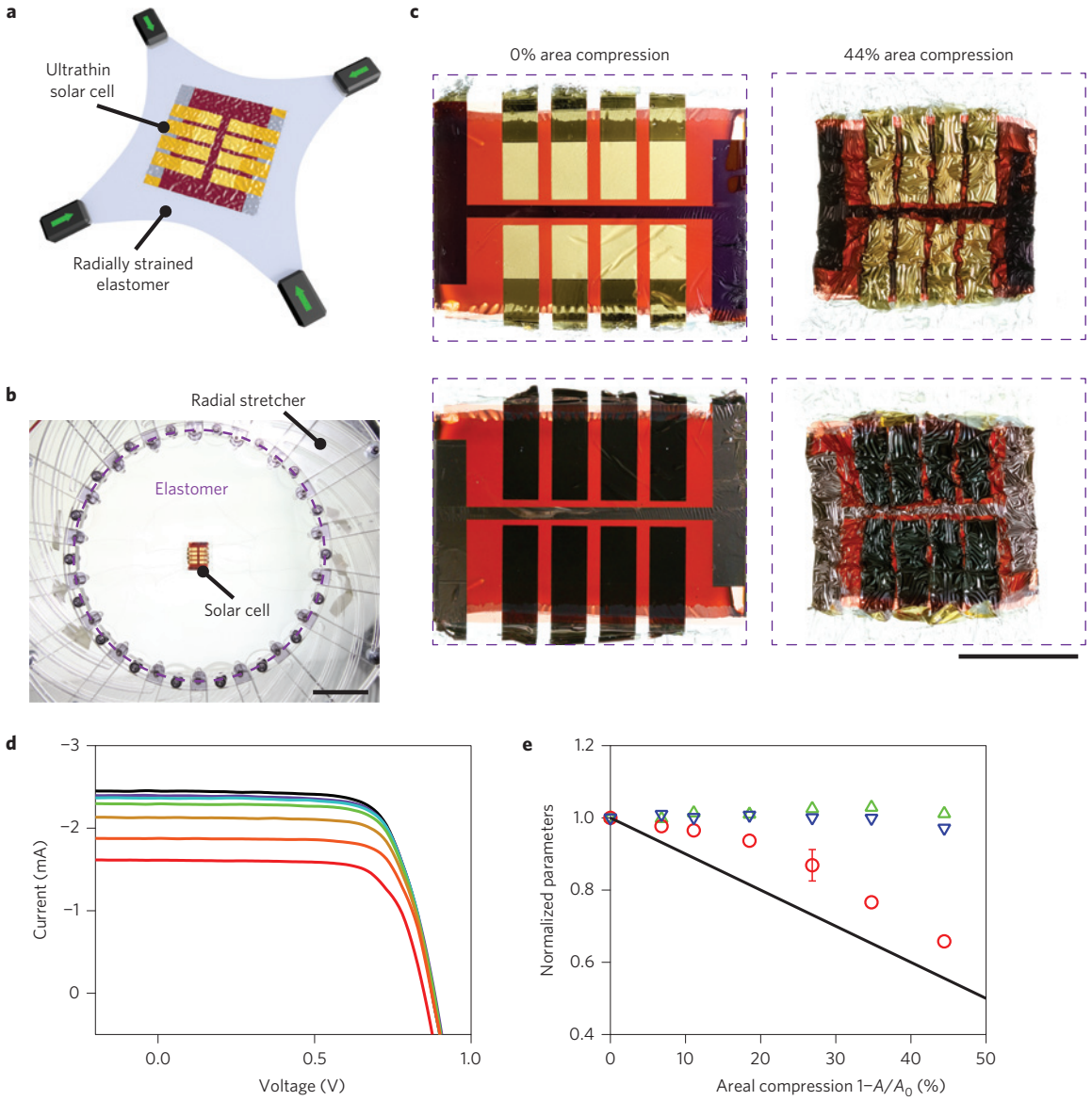

Figure 4 | Extreme compliance of ultrathin perovskite solar foils. a, Schematic of radially stretchable solar cells. The ultrathin foils are laminated to a radially pre-stretched elastomer. On relaxation of the tape, a complex microstructure of folds and wrinkles forms, allowing subsequent multidirectional deformation. **b**, Photograph of a solar panel mounted on a radial extender. Scale bar, 5 cm. **c**, Close-up images of a solar foil undergoing radial compression down to 44% in area (front side, upper row, and illuminated back side, lower row). Scale bar, 1 cm. **d**, *I*–*V* characteristics measured while the device is radially compressed. Starting from a flat configuration (black solid trace), the cell is compressed down to a 44% decrease in area (red solid trace). **e**, Solar cell performance metrics as a function of radial compression. V_{OC} (blue downward triangles) and FF (green upward triangles) remain virtually unchanged when the device is compressed. I_{SC} (red circles) decreases as the illuminated active area shrinks. As in the uniaxial case, the measured decrease in photocurrent is less than expected based on the reduction of device area (solid black line). Error bars are indicated for the J_{SC} metric for selected data points and represent statistical variations over three separate devices.

with intermediate hydrated phases forming, culminating in the reformation of PbI_2 after enough water has permeated the film[27,28]. Generation of HI, followed by formation of iodine/iodide, has been suggested as the primary root of degradation[29]. Our results with the stability enhancement given by Cr reveal an additional important degradation pathway in devices employing gold contacts. The iodine/iodide redox system is particularly reactive with gold, owing to the formation of AuI_2^- and AuI_3 (ref. 30). Indeed, iodine/iodide solutions are extensively utilized in microelectronics processing for gold etching[31]. Cr_2O_3 resists aggressive oxidizing conditions—even HNO_3 and aqua regia. Because of this excellent stability, chromium plating is used to form corrosion-resistant coatings on various metals[32]. Our Cr/Cr_2O_3 interlayer provides a buffer to shield the top contact metal from chemical etching caused by iodine liberated from the MAPI layer. The stabilizing effect of chromium oxide is universal. We find that unsealed cells with PCBM and Cr/Cr_2O_3/Al top contacts operate reasonably under ambient conditions (Supplementary Fig. 17). Identical devices that lack Cr/Cr_2O_3 fail minutes after exposure to ambient air owing to the formation of HI in the absorber layer on water ingress and the reaction of HI with aluminium, liberating H_2 gas. The formation of gas is evident from the observation of bubbling and delamination of the aluminium contact. Further experimental and theoretical considerations about the stabilizing influence of chromium oxide are found in Methods.

Weight, flexibility and conformability are pivotal to enable future technologies of wearable[33], soft[34–37], imperceptible[38,39] and

stretchable[40–43] electronics to proliferate. With a total device thickness of 3 μm, including a 1-μm-thick PU layer as mechanical protection, our ultrathin perovskite solar cells are inherently light, flexible, and conform to the surface of arbitrary three-dimensional objects. A one-step transfer process onto a pre-stretched acrylic elastomer (3M VHB) readily turns them into stretchable power sources[6,44] (Fig. 3a and Supplementary Fig. 18). Sinusoidal waves and localized high-aspect-ratio ridge wrinkles form, determined by the pre-strain of the elastomer and the flexural rigidity of the solar cells, which enable repeated stretching of the multilayer solar cell resting on the soft elastomer. A three-dimensional map of the wrinkle morphology of a sample undergoing approximately 40% compressive strain, measured by stylus profilometer, shows the formation of roughly sinusoidal folds with wavelengths from 100 μm to 300 μm and peak amplitudes of up to 140 μm (Fig. 3b). Such severe mechanical deformations require the active solar cell area to endure multiple bends into radii of curvature down to 10 μm (refs 6,45) or less. $I–V$ characteristics measured on solar foils undergoing up to 50% linear compression (equivalent to 100% tensile strain) reveal continued functioning of the photovoltaic devices without detriment (Fig. 3c,d). Whereas V_{OC} and FF do not change significantly as a function of compression, I_{SC} decreases as the illuminated active area shrinks. However, the measured decrease in photocurrent is less than expected based on the simple reduction of device area (Fig. 3c, solid black line). This suggests that the network of wrinkles and folds acts as a light-trapping microstructure[2,46]. Transmission/reflection spectra of solar foils (top metal contacts omitted) reveal that the absorptance increases as the foils are compressed and the microtexture is forming (Fig. 3e). More light is absorbed across the relevant range of wavelengths, especially in the region between the absorption onset and 600 nm. EQE measurements corroborate these findings with an enhancement of quantum efficiency for the compression-textured solar foils (Fig. 3f). With ultimately low-cost solar foils, this facile post-fabrication method of obtaining a light-trapping microstructure and solar cell performance enhancement seems promising. Such a microstructuring will require the solar cell to withstand severe mechanical deformation only once. However, we find remarkable endurance of our ultrathin perovskite solar cells even under repeated compression by 25% up to 100 cycles (Supplementary Fig. 19).

Stretchable electronics may offer unrestricted conformability with biological tissues, which will require multidimensional deformability. Transferring our ultrathin perovskite solar foils onto an elastomeric membrane with radial pre-strain (Fig. 4a,b) results in the formation of a two-dimensionally strained random wrinkle network with a much more complicated topology (Fig. 4c and Supplementary Fig. 20 and Supplementary Movie 4). The foils endure up to 44% areal compression with unaltered photovoltaic performance. We observe similar photocurrent enhancement—for example, light-trapping effects—as in the case of uniaxial compression (Fig. 4d,e).

The fabrication methods and materials engineering approaches presented herein culminate in efficient, ultrathin, light and durable solar foils with unmatched power-per-weight, mechanical flexibility, and prolonged outdoor operational stability. Mediated by solution additives to the transparent polymer electrode, low-temperature solution-processable planar perovskite solar cells are fabricated at high yield on arbitrary substrates, including thin plastic foils. The introduction of a chromium oxide/chromium interlayer renders the metallic top contacts stable to water- and oxygen-liberated corrosive species and significantly prolongs device lifetime in ambient air. These concepts are general, being readily applicable to the growing family of perovskite absorbers that may raise power-per-weight even further. Future research should be focused on improved-efficiency and moisture-resistant perovskites, exploring electrode transport materials, and alternative metals, and unifying the record efficiency of perovskite cells with the weight and flexibility demonstrated here. With high efficiency, low weight and extreme flexibility converging in this one photovoltaic technology, there seem to be few obstacles keeping perovskite solar cells grounded.

Methods

Methods and any associated references are available in the online version of the paper.

Received 27 May 2015; accepted 10 July 2015; published online 24 August 2015

References

1. http://www.solarimpulse.com (accessed 21 May 2015).
2. Green, M. A. *Third Generation Photovoltaics* (Springer, 2006).
3. Habas, S. E., Platt, H. A. S., Van Hest, M. F. a. M. & Ginley, D. S. Low-cost inorganic solar cells: From ink to printed device. *Chem. Rev.* **110,** 6571–6594 (2010).
4. Jørgensen, M. *et al.* Stability of polymer solar cells. *Adv. Mater.* **24,** 580–612 (2012).
5. Böer, K. *Handbook of the Physics of Thin-Film Solar Cells* (Springer, 2013).
6. Kaltenbrunner, M. *et al.* Ultrathin and lightweight organic solar cells with high flexibility. *Nature Commun.* **3,** 770 (2012).
7. Mitzi, D. B. in *Progress in Inorganic Chemistry* Vol. 48 (ed. Karlin, K.) 1–121 (John Wiley, 1999).
8. Stranks, S. D., Nayak, P. K., Zhang, W., Stergiopoulos, T. & Snaith, H. J. Formation of thin films of organic–inorganic perovskites for high-efficiency solar cells. *Angew. Chem. Int. Ed.* **54,** 2–11 (2015).
9. Gao, P., Gratzel, M. & Nazeeruddin, M. K. Organohalide lead perovskites for photovoltaic applications. *Energy Environ. Sci.* **7,** 2448–2463 (2014).
10. Green, M. A., Emery, K., Hishikawa, Y., Warta, W. & Dunlop, E. D. Solar cell efficiency tables (Version 45) Martin. *Prog. Photovolt. Res. Appl.* **23,** 1–9 (2015).
11. Yang, W. S. *et al.* High-performance photovoltaic perovskite layers fabricated through intramolecular exchange. *Science* **348,** 1234–1237 (2015).
12. Lee, M. M., Teuscher, J., Miyasaka, T., Murakami, T. N. & Snaith, H. J. Efficient hybrid solar cells based on meso-superstructured organometal halide perovskites. *Science* **338,** 643–647 (2012).
13. Burschka, J. *et al.* Sequential deposition as a route to high-performance perovskite-sensitized solar cells. *Nature* **499,** 316–320 (2013).
14. Liu, M., Johnston, M. B. & Snaith, H. J. Efficient planar heterojunction perovskite solar cells by vapour deposition. *Nature* **501,** 395–398 (2013).
15. http://www.geaviation.com/commercial/engines (accessed 20 May 2015).
16. Zhou, H. *et al.* Interface engineering of highly efficient perovskite solar cells. *Science* **345,** 542–546 (2014).
17. Hwang, K. *et al.* Toward large scale roll-to-roll production of fully printed perovskite solar cells. *Adv. Mater.* **27,** 1241–1247 (2015).
18. Poglitsch, A. & Weber, D. Dynamic disorder in methylammoniumtrihalogenoplumbates (II) observed by millimeter-wave spectroscopy. *J. Chem. Phys.* **87,** 6373–6378 (1987).
19. Wang, M. *et al.* Performance and stability improvement of P3HT:PCBM-based solar cells by thermally evaporated chromium oxide (CrO_x) interfacial layer. *ACS Appl. Mater. Interfaces* **2,** 2699–2702 (2010).
20. Zhan, X. *et al.* Rylene and related diimides for organic electronics. *Adv. Mater.* **23,** 268–284 (2011).
21. Huang, C., Barlow, S. & Marder, S. R. Perylene-3,4,9,10-tetracarboxylic acid diimides: Synthesis, physical properties, and use in organic electronics. *J. Org. Chem.* **76,** 2386–2407 (2011).
22. Malinkiewicz, O. *et al.* Perovskite solar cells employing organic charge-transport layers. *Nature Photon.* **8,** 128–132 (2013).
23. Wei, J., Zhao, Y., Li, H., Li, G. & Pan, J. Hysteresis analysis based on ferroelectric effect in hybrid perovskite solar cells. *J. Phys. Chem. Lett.* **5,** 3937–3945 (2014).
24. O'Regan, B. C. *et al.* Opto-electronic studies of methylammonium lead iodide perovskite solar cells with mesoporous TiO_2; separation of electronic and chemical charge storage, understanding two recombination lifetimes, and the evolution of band offsets during $J–V$ hysteresis. *J. Am. Chem. Soc.* **137,** 5087–5099 (2015).
25. Mei, A. *et al.* A hole-conductor-free, fully printable mesoscopic perovskite solar cell with high stability. *Science* **345,** 295–298 (2014).
26. Ku, Z., Rong, Y., Xu, M., Liu, T. & Han, H. Full printable processed mesoscopic $CH_3NH_3PbI_3/TiO_2$ heterojunction solar cells with carbon counter electrode. *Sci. Rep.* **3,** 3132 (2013).
27. Christians, J. A., Miranda Herrera, P. A. & Kamat, P. V. Transformation of the excited state and photovoltaic efficiency of $CH_3NH_3PbI_3$ perovskite upon controlled exposure to humidified air. *J. Am. Chem. Soc.* **137,** 1530–1538 (2015).

28. Leguy, A. *et al.* The reversible hydration of $CH_3NH_3PbI_3$ in films, single crystals and solar cells. *Chem. Mater.* **27,** 3397–3407 (2015).
29. Frost, J. M. *et al.* Atomistic origins of high-performance in hybrid halide perovskite solar cells. *Nano Lett.* **14,** 2584–2590 (2014).
30. Davis, A., Tran, T. & Young, D. R. Solution chemistry of iodide leaching of gold. *Hydrometallurgy* **32,** 143–159 (1993).
31. Williams, K. R., Gupta, K. & Wasilik, M. Etch rates for micromachining processing—Part II. *J. Microelectromech. Syst.* **12,** 761–778 (2003).
32. Downing, J. H., Deeley, P. D. & Fichte, R. Chromium and chromium alloys. *Ullmann's Encycl. Ind. Chem.* **9,** 131–155 (2012).
33. Cherenack, K. & VanPieterson, L. Smart textiles: Challenges and opportunities. *J. Appl. Phys.* **112,** 091301 (2012).
34. Hammock, M. L., Chortos, A., Tee, B. C.-K., Tok, J. B.-H. & Bao, Z. 25th anniversary article: The evolution of electronic skin (E-Skin): A brief history, design considerations, and recent progress. *Adv. Mater.* **25,** 5997–6038 (2013).
35. Bauer, S. *et al.* 25th anniversary article: A soft future: From robots and sensor skin to energy harvesters. *Adv. Mater.* **26,** 149–162 (2013).
36. Wang, Q., Gossweiler, G. R., Craig, S. L. & Zhao, X. Cephalopod-inspired design of electro-mechano-chemically responsive elastomers for on-demand fluorescent patterning. *Nature Commun.* **5,** 4899 (2014).
37. Keplinger, C. *et al.* Stretchable, transparent, ionic conductors. *Science* **341,** 984–987 (2013).
38. Kim, D.-H. *et al.* Epidermal electronics. *Science* **333,** 838–843 (2011).
39. Kaltenbrunner, M. *et al.* An ultra-lightweight design for imperceptible plastic electronics. *Nature* **499,** 458–463 (2013).
40. Rogers, J. A., Someya, T. & Huang, Y. Materials and mechanics for stretchable electronics. *Science* **327,** 1603–1607 (2010).
41. Sekitani, T. & Someya, T. Stretchable, large-area organic electronics. *Adv. Mater.* **22,** 2228–2246 (2010).
42. Wagner, S. & Bauer, S. Materials for stretchable electronics. *MRS Bull.* **37,** 207–213 (2012).
43. Jablonski, M., Bossuyt, F., Vanfleteren, J., Vervust, T. & De Vries, H. Reliability of a stretchable interconnect utilizing terminated, in-plane meandered copper conductor. *Microelectron. Reliab.* **53,** 956–963 (2013).
44. Lipomi, D. J. & Bao, Z. Stretchable, elastic materials and devices for solar energy conversion. *Energy Environ. Sci.* **4,** 3314–3328 (2011).
45. White, M. S. *et al.* Ultrathin, highly flexible and stretchable PLEDs. *Nature Photon.* **7,** 811–816 (2013).
46. Kim, J. B. *et al.* Wrinkles and deep folds as photonic structures in photovoltaics. *Nature Photon.* **6,** 327–332 (2012).

Acknowledgements

This work was supported by the ERC Advanced Investigators Grant 'Soft-Map' to S.B. and the FWF Wittgenstein Award (Solare Energie Umwandlung Z222-N19) to N.S.S. H.G. acknowledges funding through the FWF grant Nr. J3317-N27. We thank J. Duchoslav for XPS measurements. The authors are indebted to S. Schausberger, M. Krause, H. Heilbrunner and T. Stockinger for fruitful scientific discussions.

Author contributions

M.K. conceived and supervised the research. G.A. developed the MAPI precursor and optimized the coating recipe. G.A., E.D.G., M.K. and L.L. fabricated solar cells. G.A., D.H.A., M.D., E.D.G., H.G., M.K., M.C.S. and M.S.W. characterized devices. M.D., M.K. and R.S. designed outdoor demos. S.B., E.D.G., M.K. and M.S.W. analysed data, designed figures, and wrote the manuscript with comments from all co-authors. N.S.S. and S.B. coordinated the project.

Additional information

Supplementary information is available in the online version of the paper. Reprints and permissions information is available online at www.nature.com/reprints. Correspondence and requests for materials should be addressed to M.K.

Competing financial interests

The authors declare no competing financial interests.

Methods

Device fabrication. Glass slides (26 mm by 26 mm) coated with a thin layer of PDMS (Sylgard 184 Silicone Elastomer, Dow Corning, spin-coated at 4,000 r.p.m. for 60 s from a solution of 10:1 w/w PDMS base to hardener, diluted 1:2 in hexane, and subsequently annealed at 150 °C for 30 min), served as reusable support for the 1.4-μm-thick PET foil (Mylar 1.4 CW02). The polymer film adheres through weak van der Waals forces only, enabling all subsequent processing steps (spin coating, thermal annealing and vacuum evaporation). After fabrication, the devices can be peeled off the support without causing damage[47]. Pre-patterned ITO-coated glass (26 mm by 26 mm) served as reference substrates. A dispersion of PEDOT:PSS was prepared from stock Clevios PH1000 with 5 vol% dimethylsulphoxide (DMSO) and 0.5 vol% Zonyl FS-300 fluorosurfactant (Fluka). This formulation was spun onto the PET foil or the glass/ITO at 1,000 r.p.m. for 40 s, followed by 2,000 r.p.m. for 10 s, and subsequently annealed at 110 °C for 10 min. The PEDOT:PSS films were briefly rinsed with 2-Propanol to remove any excess surfactant on the surface, and dried for another 10 min at 110 °C. The MAPI perovskite layer was prepared via a single-step process from solution, which we have optimized to be robust in ambient laboratory conditions without the need for temperature/humidity control: a solution in dimethylformamide (DMF) of 0.5 $PbCl_2$ + 0.5 PbI_2 + 2.2 CH_3NH_3I (by molar ratio) is prepared to give a total of 640 mg ml^{-1}. Following spin casting at 1,800 r.p.m. for 15 s and 2,000 r.p.m. for 5 s, the substrates are annealed at 110 °C for 20 min in air. The final stoichiometry of the perovskite in terms of iodide and chloride content was not evaluated; the exact composition of perovskites originating from mixed halide precursor solutions is an ongoing subject of debate[8]. Next, the samples are transferred to a vacuum chamber where PTCDI is evaporated at a rate of 3–5 Å s^{-1} at a base pressure of 1 × 10^{-6} mbar to a total thickness of ~100 nm. PTCDI was obtained from BASF in the form of the commercial Pigment Red 179 (Paliogen Rot), and before use was resublimed three times in a temperature gradient vacuum furnace to give ultrapure material. Alternatively to PTCDI, solution-processed PCBM was used for comparison, which in turn was spin cast at 1,500 r.p.m. for 30 s from a 2 wt% solution in 1:1 chlorobenzene:chloroform. Following deposition of the n-type buffer layer, the samples are transferred to a metallization chamber (located in a non-inert environment, re-pressurized with nitrogen gas), where a 10 nm-thick Cr layer is evaporated using 2-inch chromium plated tungsten rods (Kurt J. Lesker Company) at a base pressure of ~2 × 10^{-6} mbar, with a rate of 0.3–1 Å s^{-1}. An important consideration is the formation of the oxide layer under our experimental conditions: assuming the partial pressure of O_2 in the evaporation chamber at 2 × 10^{-6} mbar (p_{O_2} = 4.6 × 10^{-7} mbar), 10^{15} sites cm^{-2}, and a formation factor of 1 (each collision of O_2 molecule with the Cr surface leads to a reaction), it takes 28 s for a continuous oxide layer to form. As the evaporation of a 10 nm film lasts at least 150 s, an oxide forms under these conditions, as confirmed by XPS (Supplementary Fig. 2). Thermal evaporation of chromium under similar conditions onto a polymer photovoltaic was reported to provide an electron-selective layer of Cr_2O_3 (ref. 19). We note that the successful formation of Cr_2O_3 can depend on the vacuum system used, and may not proceed equivalently under very inert conditions. We find that the Cr-plated tungsten rods used as the thermal evaporation sources in our system appear deep green already after the first use as a result of oxidation, providing simple evidence for successful oxide formation. The enthalpies of formation of Cr_2O_3 (H_f = −1,128 kJ mol^{-1}) versus CrI_3 (H_f = −205 kJ mol^{-1}) explain the stability of the chromium oxide interlayer in contact with iodine/iodide. Moreover chromium oxide is stable against both strong (such as HI) and weak acids. Next, a ~100 nm layer of gold, copper or aluminium was evaporated onto the chromium layer. Devices using only chromium contacts were functional; however, owing to the comparatively high resistivity of the chromium metal the fill factor suffered. The combination of a highly conducting Au, Cu, or Al layer on top of a thin Cr/Cr_2O_3 interlayer significantly improves device performance. Completed foil devices were covered with a spray-painted PU resin (CRC Kontakt Chemie Urethan 71) to give a 1 μm-thick polymeric layer that places the diode stack into the neutral mechanical plane, and to provide a basic protection against mechanical damage. The PU coating was allowed to crosslink at room temperature for roughly 24 h before outdoor experiments and stretching tests.

Device characterization. Optical microscopy images were obtained in transmission mode using a Nikon Eclipse LV100ND microscope with up to ×400 magnification. Ultraviolet–visible–near infrared transmission and reflection spectra were collected using a Perkin-Elmer Lambda 950 spectrometer with a modular 150-mm integrating sphere accessory. X-ray diffraction was conducted in $\omega/2\theta$ geometry using a Bruker AXS diffractometer with Fe Kα irradiation. A stretcher apparatus was constructed to allow compression of foils *in situ* with optical measurements. The devices with an active area of 0.14–0.15 cm^2 were characterized in the dark and under illumination of a LOT-QD solar simulator (AM 1.5 Global spectrum with 1,000 W m^{-2} intensity calibrated with a silicon reference diode) at a scan rate of 20 mV s^{-1} (unless otherwise noted), both in forward and reverse scan directions. Reference devices on glass/ITO and glass-supported foil cells were initially characterized using a metal shadow mask with a 0.135 cm^2 aperture to define the active device area. For freestanding foils, device areas were taken from optical microscopy images. I–V characteristics were recorded using a Keithley 2400 source meter. MPP tracking was carried out with a custom LabView program, following an industry-standard perturb and observe algorithm (block diagram depicted in Supplementary Fig. 19). Solar cells on foil were initially characterized on their rigid support (J–V scans and MPP tracking up to 1,000 s). Subsequent long-term tests were conducted on freestanding foils. Releasing the foils from their rigid support has no negative impact on their initial performance. Air stability tests were carried out in ambient laboratory atmosphere without humidity or temperature control. The solar cells were not actively cooled. External quantum efficiencies (EQEs) were recorded by using a lock-in amplifier (SR830, Stanford Research Systems) and a Jaissle 1002 potentiostat functioning as a preamplifier. The devices were illuminated by monochromatic light from a xenon lamp passing through a monochromator (Oriel Cornerstone) with intensities in the range 10–100 μW. A filter wheel holding long-pass filters and a mechanical chopper was mounted between the xenon lamp and the monochromator. Chopping frequencies in the range 10–200 Hz were used. A calibrated silicon diode (Hamamatsu S2281) was used as a reference. A halogen lamp (Philips 50 W, 12 V) provided a variable white light bias to the solar cells while the EQE was measured. AFM measurements were conducted on a Dimension 3100 system (Digital instruments) operating in tapping mode. Surface and cross-section SEM measurements were made using a ZEISS 1540XB CrossBeam Scanning microscope equipped with a focused ion-beam (FIB) module. Layer thicknesses were determined by a Bruker DektakXT stylus profilometer and by cross-sectional TEM images using a Jeol JEM-2200FS at 200 kV. XPS analysis was carried out on a Theta Probe (Thermo Scientific) with a monochromatic Al Kα source at 1486.6 eV and a spot size of 400 μm^2. A dual flood gun was used for charge neutralization.

Power-per-weight. The power-per-weight (also referred to as specific weight or specific power in the literature) is defined as the ratio of the output power per unit area of the solar cell under standard solar irradiation (AM 1.5 Global spectrum with 1,000 W m^{-2} intensity) to the weight of the solar cell per unit area. The scaling area cancels, and the resulting W g^{-1} are reported. The ultrathin perovskite cells reported in this work have a stabilized PCE of 12% at a weight of 5.2 g m^{-2} (4.6 g m^{-2} without PU capping). This equates to a specific weight (watts produced under AM 1.5 1,000 W m^{-2} irradiation/weight) of 23 W g^{-1} (26 W g^{-1} without PU). The power-per-weight of the other solar cells compared in Fig. 1d were calculated from published academic results. Further detailed considerations on power-per-weight calculations can be found in the Supplementary Information.

Neutral mechanical plane and flexural rigidity. We calculate the position b of the neutral mechanical plane (zero-strain position) of a multilayer stack with the nth layer atop the first layer on the bottom according to ref. 48:

$$b = \frac{\sum_{i=1}^{n} E_i t_i \left[\sum_{j=1}^{i} t_j \frac{t_i}{2}\right]}{\sum_{i=1}^{n} E_i t_i}$$

where E_i and t_i denote the Young's moduli and thicknesses of the individual layers. For the ultrathin solar foils (n = 7, 1.4 μm PET / 130 nm PEDOT:PSS / 300 nm MAPI / 90 nm PTCDI / 10 nm Cr / 100 nm Au / 1 μm PU) the elastic moduli are E_{PET} = 2 GPa, E_{PEDOT} = 1 GPa, E_{MAPI} = 100 GPa, E_{PTCDI} = 2.3 GPa, E_{Cr} = 294 GPa, E_{Au} = 79 GPa and E_{PU} = 0.4 GPa. This places the neutral mechanical plane at a distance b of 1.7 μm from the bottom surface of the PET substrate, into the centre of the polycrystalline MAPI layer.

The high stretchability reported here is based on out-of-plane wrinkling enabled by the low flexural rigidity D of the ultrathin solar foils. D is a measure of the flexibility of the ultrathin perovskite cells[48]:

$$D = \sum_{i=1}^{n} E_i t_i \left(b \sum_{j=1}^{i} t_j\right)^2 + \sum_{i=1}^{n} E_i t_i^2 \left(b \sum_{j=1}^{i} t_j\right) + \frac{1}{3} \sum_{i=1}^{n} E_i t_i^3$$

for a multilayer stack of n layers. This results in D = 4.6 × 10^{-9} Pa m^3 for our solar foils, which is five orders of magnitude lower than that of conventional, 125-μm thick polymer foils (≈5 × 10^{-4} Pa m^3).

Stretchable solar cells. Ultrathin solar cells were transferred to a pre-stretched 3M VHB 4905 acrylic elastomer. Uniaxial compression/re-stretching was carried out on a custom-built stretching stage (Supplementary Fig. 21). Cyclic stretching was carried out on an automated stretching stage (Supplementary Fig. 19b). Biaxial stretching was performed on a radial extender[49] depicted in Fig. 4a,b. Areas were extracted from optical images found in

Supplementary Figs 18 and 20. All experiments were carried out in ambient air under ~0.8 sun illumination.

References

47. Drack, M. *et al.* An imperceptible plastic electronic wrap. *Adv. Mater.* **27,** 34–40 (2014).
48. Kim, D.-H. *et al.* Stretchable and foldable silicon integrated circuits. *Science* **320,** 507–511 (2008).
49. Schausberger, S. E. *et al.* Cost-efficient open source desktop size radial stretching system with force sensor. *IEEE Access* **3,** 556–561 (2015).